NEOPLASMA accepted, ahead of print manuscript
Cite article as https://doi.org/10.4149/neo_2025_250403N151

Running title: ANLN knockdown impairs ribosome biogenesis in NPC

ANLN knockdown inhibits nasopharyngeal carcinoma proliferation and is associated with impaired ribosome biogenesis

Zhengxin Zhu, Li Fu, Xue Bai, Wanqing Zhang, Songtao Liu, Hongli Min, Yuehui Liu*

Department of Otorhinolaryngology Head and Neck Surgery, The Second Affiliated Hospital, Jiangxi Medical College, Nanchang University, Nanchang, Jiangxi, China

*Correspondence: liuyuehuiclark@21cn.com

Received April 3, 2025 / Accepted July 2, 2025

Anillin (ANLN), an actin-binding protein, has been implicated in tumorigenesis across various cancers; however, its role in nasopharyngeal carcinoma (NPC) remains largely undefined. In this study, we analyzed ANLN expression using TCGA, CPTAC, and GEO datasets, and confirmed its overexpression in NPC tissues and cell lines through qRT-PCR, western blotting, and immunohistochemistry. High ANLN expression correlated with advanced clinical stage and poor overall survival. Functional assays, including CCK-8 and colony formation, demonstrated that ANLN knockdown suppressed NPC cell proliferation *in vitro*, while xenograft models confirmed reduced tumor growth *in vivo*. RNA sequencing and gene set enrichment analysis revealed that ANLN knockdown was associated with downregulation of ribosome biogenesis pathways. Puromycin incorporation assays and transmission electron microscopy further supported impaired protein synthesis and nucleolar disruption following ANLN depletion. These findings suggest that ANLN promotes NPC progression by maintaining ribosome biogenesis and protein synthesis and may serve as a novel prognostic biomarker and therapeutic target.

Key words: ANLN; nasopharyngeal carcinoma; ribosome biogenesis; protein synthesis; tumor proliferation

Nasopharyngeal carcinoma (NPC) is a malignant epithelial tumor arising from the nasopharyngeal mucosa, with a particularly high prevalence in Southern China and Southeast Asia [1-3]. Despite advances in radiotherapy and chemotherapy, the prognosis for patients with advanced or recurrent NPC remains unsatisfactory due to distant metastasis and treatment resistance [4, 5]. Understanding the molecular mechanisms driving NPC progression is crucial for identifying novel therapeutic targets and improving patient outcomes.

Anillin (ANLN) is an actin-binding protein that plays a key role in cytokinesis and the maintenance

of cell structure [6-8]. Recent studies have demonstrated that ANLN is aberrantly overexpressed in various human malignancies, including breast, bladder, and pancreatic cancers, where it has been associated with enhanced tumor proliferation, invasion, and poor prognosis [9-13]. Beyond its canonical role in cytoskeletal regulation and cell division, emerging evidence suggests that ANLN may also be involved in nuclear processes such as transcriptional control and chromatin remodeling [10, 14], hinting at broader functional roles in cancer biology.

Ribosome biogenesis is a fundamental and tightly regulated process responsible for the production of ribosomes, which are essential for protein synthesis and cell growth [15, 16]. Cancer cells frequently exhibit upregulated ribosome biogenesis to sustain their increased protein demands [17-19]. Although deregulated ribosome biogenesis has been recognized as a hallmark of cancer, the regulatory mechanisms that link oncogenic drivers like ANLN to this process in NPC remain largely uncharacterized. Given the high metabolic demands and rapid proliferation of NPC cells, understanding how ribosome biogenesis contributes to NPC tumorigenesis may reveal vulnerabilities that can be therapeutically targeted.

In this study, we aimed to investigate the expression and functional role of ANLN in NPC. Using integrative bioinformatics analyses from public datasets, complemented by experimental validation in NPC cell lines and clinical specimens, we evaluated ANLN expression and its prognostic value. We further assessed the impact of ANLN knockdown on NPC cell proliferation both *in vitro* and *in vivo*, and investigated its relationship with ribosome biogenesis and protein synthesis. Our findings suggest a novel oncogenic role for ANLN in NPC progression and support its potential as a prognostic biomarker and therapeutic target.

Patients and methods

Public datasets and bioinformatics analysis. The UALCAN online portal (http://ualcan.path.uab.edu/) [20, 21], which integrates data from The Cancer Genome Atlas (TCGA) and Clinical Proteomic Tumor Analysis Consortium (CPTAC), was used to evaluate ANLN mRNA and protein expression.

Three datasets from the Gene Expression Omnibus (GEO) database [22] were analyzed. GSE12452 and GSE61218 were employed to assess differential ANLN expression between NPC tissues and normal nasopharyngeal mucosa. GSE102349, containing gene expression profiles with clinical annotations, was used to explore the association between ANLN expression and clinical stage as

well as overall survival.

Clinical samples. The use of human tissue samples was approved by the Ethics Committee of the Second Affiliated Hospital of Nanchang University (Approval No. 2022143). Written informed consent was obtained from all patients or their legal guardians prior to sample collection.

Tumor tissues and paired adjacent non-cancerous tissues were collected from six patients diagnosed with NPC who received treatment at the Department of Otolaryngology-Head and Neck Surgery of the same hospital.

Inclusion criteria: 1) Tumor tissues were obtained from neoplastic lesions in the nasopharynx, with NPC confirmed by pathological biopsy; 2) Patients had not received radiotherapy or chemotherapy before sample collection. Adjacent non-cancerous tissues were defined as tissues located 1-3 cm from the visible tumor margin without grossly evident tumor nodules, including both the epithelial layer and the underlying lamina propria.

Exclusion criteria: 1) Patients with other concurrent malignant tumors; 2) Patients with psychiatric disorders or severe coagulation dysfunction hat hindered safe biopsy collection.

Cell culture and transfection. Human NPC cell lines (CNE-1, CNE-2Z, 5-8F, 6-10B) and immortalized nasopharyngeal epithelial cell line (NP69) were obtained from the Cell Bank of the Chinese Academy of Sciences (Shanghai, China). Cells were cultured in DMEM or RPMI-1640 medium, supplemented with 10% fetal bovine serum (FBS), at 37 °C in a humidified incubator containing 5% CO_2 .

Lentiviruses encoding short hairpin RNAs targeting ANLN (shANLN) and negative control (shNC) were purchased from Focus Bioscience Inc. (Shanghai, China). Small interfering RNAs (siRNAs) targeting ANLN (siANLN) were also obtained from the same company. Transfection was conducted according to the manufacturer's protocols.

qRT-PCR. Total RNA was isolated using TRIzol reagent (TransGen Biotech, China). Complementary DNA (cDNA) was synthesized using the TransScript® One-Step gDNA Removal and cDNA Synthesis SuperMix (TransGen Biotech, China). Quantitative PCR was performed with TB Green® Premix Ex Taq™ II (TaKaRa, Japan) using a real-time PCR system (Applied Biosystems, USA). The primer sequences were as follows: ANLN: forward 5′- TGG CAT CGA AGA TGG TGT GT -3′, reverse 5′- AGA GTG TGT CCC TGC ATT GG -3′; GAPDH: forward 5′-ACC TGA CCT GCC GTC TAG AA -3′, reverse 5′-TCC ACC ACC CTG TTG CTG TA -3′. Relative expression was calculated using the 2^-ΔΔCt method.

Western blot. Total protein was extracted using RIPA lysis buffer (Applygen, China) supplemented with protease and phosphatase inhibitors (Applygen, China). Protein concentration was measured using a BCA Protein Assay Kit (Solarbio, China). Equal amounts of protein were separated by 10% SDS-PAGE and transferred onto PVDF membranes (Beyotime, China). Membranes were blocked in 5% non-fat milk for 2 h and incubated overnight at 4 °C with primary antibodies: Anti-ANLN (#66643-1-lg, Proteintech, China); Anti-GAPDH (#60004-1-Ig, Proteintech, China). After washing, membranes were incubated with HRP-conjugated secondary antibodies (#SA00001-1, Proteintech, China) for 1 h at room temperature. Detection was performed using ECL chemiluminescence reagent (Beyotime, China), and signal intensities were analyzed with Image Lab 5.2.1 software (Bio-Rad, USA).

Immunohistochemistry (IHC). Paraffin-embedded tissue sections (5 μm thick) were deparaffinized and rehydrated. Antigen retrieval was performed using sodium citrate buffer (pH 6.0). Sections were blocked in BSA for 30 min and incubated overnight at 4 °C with the following primary antibodies: Anti-ANLN (1:100, #sc-271814, Santa, USA), Anti-Ki67 (1:200, #27309-1-AP, Proteintech, China). After incubation with HRP-conjugated secondary antibodies (Proteintech, China) for 30 min, the signal was developed using DAB (Solarbio, China) and counterstained with hematoxylin. Images were captured using an Olympus microscope (Japan).

Quantitative assessment of immunohistochemical staining was conducted using a semi-quantitative scoring system. Staining intensity was graded on a 4-point scale: 0 (no staining), 1 (light yellow, weak positive), 2 (brownish-yellow, moderate positive), and 3 (dark brown, strong positive). The percentage of positively stained cells was scored as follows: 1 (≤ 25%), 2 (26-50%), 3 (51-75%), and 4 (> 75%). The final IHC score was obtained by multiplying the intensity and percentage scores, yielding a total score ranging from 0 to 12. All sections were scored independently by two experienced pathologists in a blinded manner.

Proliferation experiment. CCK-8 assay: Cells were seeded in 96-well plates (2×10^3 cells/well), and cultured for 0, 24, 48, and 72 h, followed by incubation with CCK-8 solution (HanBio, China) for 2 hours. Absorbance was measured at 450 nm using a microplate reader.

Colony formation assay: A total of 500 cells/well were seeded in 6-well plates and cultured for 14 days. Colonies were fixed with 4% paraformaldehyde (Solarbio, China), stained with 0.5% crystal violet (Solarbio, China), and manually counted. Colony counting was performed using ImageJ 1.54. A colony was defined as a cluster of ≥ 50 cells.

RNA Sequencing (RNA-seq). Total RNA was extracted from NPC cells transfected with shNC or shANLN using TRIzol reagent (TransGen Biotech, China), following the manufacturer's protocol. The quantity and integrity of RNA were assessed using a NanoDrop 2000 spectrophotometer (Thermo Fisher Scientific, USA). RNA samples with an RNA integrity number (RIN) ≥ 7.0 were selected for library construction.

mRNA libraries were constructed using the NEBNext® Ultra™ II RNA Library Prep Kit for Illumina® (New England Biolabs, USA) and sequenced on an Illumina NovaSeq 6000 platform (Illumina, USA) with 150 bp paired-end reads. Raw sequencing data were subjected to quality control using FastQC (v0.11.9), and low-quality reads were removed using Trimmomatic (v0.39). Clean reads were aligned to the human genome reference (GRCh38) using HISAT2 (v2.2.1), and gene expression quantification was performed with featureCounts (v2.0.1). Differential gene expression analysis between shANLN and shNC groups was conducted using DESeq2 in R software. Genes with $|\log_2(\text{fold change})| \geq 1$ and adjusted p-value < 0.05 were considered significantly differentially expressed.

Gene Set Enrichment Analysis (GSEA). GSEA was performed using GSEA software (v4.3.2) from the Broad Institute (http://www.gsea-msigdb.org/). The expression dataset was ranked based on the signal-to-noise ratio, and predefined gene sets from the Molecular Signatures Database (MSigDB, v2023.1) were used. The number of permutations was set to 1000, and gene sets with nominal p-value < 0.05 and false discovery rate (FDR) < 0.25 were considered significantly enriched. Enrichment plots and normalized enrichment scores (NES) were used to visualize the results.

Puromycin incorporation assay. NPC cells (with or without ANLN knockdown) were treated with puromycin (10 μg/ml, Beyotime, China) for 30 min at 37 °C. Cells were lysed using RIPA buffer, and equal amounts of protein were subjected to SDS-PAGE. Membranes were incubated with anti-puromycin antibody (#A23031, Abclonal, China) and subjected to Western blot analysis to detect nascent polypeptides.

Transmission electron microscopy (TEM). Cells were fixed in 2.5% glutaraldehyde (Servicebio, China) in 0.1 M phosphate buffer (pH 7.4) at 4 °C overnight. After rinsing, samples were post-fixed with 1% osmium tetroxide, dehydrated through graded ethanol, and embedded in epoxy resin. Ultrathin sections (60-90 nm) were stained with uranyl acetate and lead citrate, and examined using a Hitachi transmission electron microscope (Japan).

Nude mouse xenograft model. To minimize variability due to male territorial aggression, Female BALB/c nude mice (4 weeks old, SPF grade; purchased from SPF Biotechnology Co., Ltd., China) were randomly divided into three groups (n=5/group). Each mouse was injected subcutaneously into the right flank with 1×10^6 5-8F cells stably expressing shNC, shANLN-1, or shANLN-2 in 100 μl of PBS:Matrigel (1:1). Tumor dimensions were measured every three days using a digital caliper, and tumor volume was calculated as $0.5 \times \text{length} \times \text{width}^2$. After 21 days, mice were euthanized, and tumors were excised, photographed, and weighed. Tissues were fixed in 10% neutral formalin for further histological analysis.

All animal experiments were approved by the Institutional Animal Care and Use Committee of Nanchang Royo Biotech Co., Ltd. (Approval No. RYE2024061102) and conducted in accordance with the ARRIVE guidelines and national regulations on the care and use of laboratory animals.

Statistical analysis. All data are presented as mean±standard deviation (SD). Statistical analysis was performed using SPSS 21.0, GraphPad Prism 10.2, and R 4.4.1. Each experiment was conducted in at least three independent biological experiments (n=3), with three technical replicates per experiment. Comparisons between two groups were analyzed using Student's t-test or Wilcoxon test, as appropriate. One-way ANOVA was used for multi-group comparisons. Kaplan–Meier survival curves were compared using the log-rank test. A p-value < 0.05 was considered statistically significant.

Results

ANLN is overexpressed in multiple cancers and associated with poor prognosis in NPC. To systematically evaluate the expression profile of ANLN across human malignancies, we first performed a pan-cancer analysis using TCGA and CPTAC datasets. ANLN mRNA levels were found to be significantly upregulated in multiple cancer types, including breast invasive carcinoma (BRCA), cervical squamous cell carcinoma (CESC), cholangiocarcinoma (CHOL), colon adenocarcinoma (COAD), esophageal carcinoma (ESCA), and head and neck squamous cell carcinoma (HNSC) (Figure 1A). CPTAC proteomics data corroborated these findings, showing elevated ANLN protein expression in breast, colon, and head and neck tumors compared to normal tissues (Figure 1B).

Focusing on NPC, we further analyzed expression patterns using GEO datasets. In GSE12452 and GSE61218, ANLN expression was markedly higher in NPC tissues than in normal nasopharyngeal

mucosa (Figures 1C, 1D). Additionally, analysis of the GSE102349 cohort revealed that ANLN expression positively correlated with advanced clinical staging (Figure 1E) and was associated with significantly poorer overall survival (Figure 1F), implicating ANLN as a potential prognostic biomarker in NPC.

ANLN is highly expressed in NPC cell lines and clinical specimens. To validate these findings experimentally, we measured ANLN expression in NPC cell lines and clinical samples. qRT-PCR and Western blot analyses confirmed that ANLN mRNA and protein levels were significantly upregulated in NPC cell lines (5-8F, 6-10B, CNE-1, and CNE-2Z) compared to the normal nasopharyngeal epithelial cell line NP69 (Figures 2A-2C). Immunohistochemical staining of paired NPC tumor and adjacent non-tumor tissues further revealed increased ANLN immunoreactivity in tumor samples (Figures 2D, 2E).

Knockdown of ANLN inhibits NPC cell proliferation *in vitro*. Having confirmed ANLN overexpression, we next explored its functional role in tumor cell proliferation. Using lentiviral vectors expressing ANLN-specific shRNAs, we successfully knocked down ANLN expression in 5-8F and 6-10B cells. Western blot analysis confirmed effective ANLN knockdown compared to the control group (shNC) (Figures 3A, 3B). Functionally, CCK-8 assays revealed that ANLN knockdown significantly reduced cell proliferation over 24, 48, and 72 hours (Figure 3C). Similarly, colony formation assays showed a marked decrease in the number of colonies in ANLN knockdown cells (Figures 3D, 3E), indicating that ANLN contributes to the proliferative capacity of NPC cells.

Knockdown of ANLN inhibits tumor growth *in vivo*. To determine whether these *in vitro* effects could be recapitulated *in vivo*, we established a subcutaneous xenograft model in nude mice using control and ANLN-knockdown NPC cells. Tumor volume measurements over time showed significantly smaller tumors in the shANLN-1 and shANLN-2 groups compared to the shNC group (Figure 4D), although body weight remained consistent across groups (Figure 4C). Final tumor weights were significantly lower in the ANLN knockdown groups (Figures 4A, 4B). Ki-67 immunohistochemical staining revealed reduced proliferative activity in ANLN-silenced tumors (Figure 4E), supporting the tumor-suppressive effect of ANLN knockdown *in vivo*.

Knockdown of ANLN impairs ribosome biogenesis and protein synthesis. To explore the mechanisms by which ANLN promotes NPC progression, we performed RNA-seq analysis on ANLN knockdown cells. List of differentially expressed genes was provided in Supplementary Table S1 and the top-ranked differentially expressed genes were summarized in Supplementary

Table S2. Volcano plots and heatmap of differentially expressed genes were presented in Supplementary Figure S1. Gene Set Enrichment Analysis (GSEA) revealed significant downregulation of the ribosome biogenesis pathway (GO:0042254), with a reduced normalized enrichment score (NES) indicating impaired ribosomal activity (Figure 5A). The leading-edge genes enriched were shown in Supplementary Table S3.

In line with transcriptomic results, puromycin incorporation assays demonstrated reduced levels of nascent protein synthesis in ANLN knockdown cells compared to controls (Figure 5B, Supplementary Figure S2), indicating suppressed mRNA translation. Transmission electron microscopy further revealed ultrastructural changes in nucleoli, including reduced size and decreased ribosomal granule density within ANLN knockdown cells (Figures 5C, 5D), corroborating the RNA-seq findings.

Discussion

Our study uncovers a previously underappreciated oncogenic role for ANLN in NPC, supported by integrative bioinformatics, *in vitro* and *in vivo* validation, and mechanistic investigation. We first demonstrated that ANLN is broadly upregulated across various human malignancies, including head and neck squamous cell carcinoma, through pan-cancer transcriptomic and proteomic analyses. Specifically, ANLN expression was significantly elevated in NPC tissues and cell lines compared to normal controls, and its expression positively correlated with clinical stage and poor prognosis, suggesting its potential as a prognostic biomarker. Functional assays revealed that ANLN knockdown significantly suppressed NPC cell proliferation and colony-forming ability *in vitro*, while also reducing tumor growth and Ki-67 expression in a xenograft mouse model, indicating its critical role in sustaining tumor progression. Mechanistically, transcriptomic profiling of ANLN-silenced cells identified a marked downregulation of the ribosome biogenesis pathway, a finding that was further supported by reduced nascent protein synthesis and impaired nucleolar structure observed via puromycin labeling and electron microscopy. These results collectively suggest that ANLN promotes NPC progression at least in part by maintaining ribosome biogenesis and protein synthesis, thus supporting the biosynthetic and proliferative demands of tumor cells.

Historically, ANLN has been described as a cytoskeletal-associated factor essential for cytokinesis and cell migration [23, 24]. Its overexpression has been reported in breast, bladder, and pancreatic cancers, where it primarily regulates actomyosin contractility and mitotic progression [25-28].

However, these studies have largely focused on its roles during cell division and rarely explored its functions in the interphase. Interestingly, previous research has shown that ANLN predominantly localizes to the nucleus during interphase [28], but its nuclear role has remained poorly defined. In contrast, our study reveals that ANLN regulates ribosome biogenesis-a nuclear and nucleolar process-thereby identifying a novel function for ANLN beyond its established cytoplasmic roles. We found that knockdown of ANLN not only reduced nascent protein synthesis, but also disrupted nucleolar architecture, as evidenced by puromycin incorporation assays and electron microscopy. These findings significantly expand the functional repertoire of ANLN.

The nucleolus is the site of rRNA transcription, processing, and assembly of ribosomal subunits [29, 30]. Recent studies have highlighted the centrality of nucleolar stress in tumor suppression and therapeutic response. For example, Brown et al. [31] showed that elevated nucleolar activity predicts poor prognosis in various malignancies, while Ferreira et al. [32] demonstrated that targeting RNA polymerase I-mediated rRNA synthesis using the selective inhibitor PMR-116 effectively suppressed tumor growth across multiple cancer types. Based on our results, we hypothesize that ANLN may influence ribosome biogenesis, possibly through effects on chromatin accessibility at rDNA loci or by scaffolding nucleolar proteins such as fibrillarin and nucleolin-key players in rRNA processing. While we did not directly map these interactions, the convergence of transcriptional, translational, and structural data supports a potential functional association between ANLN and nucleolar activity.

This study presents several novel contributions. It is the first to connect ANLN with ribosome biogenesis in the context of solid tumors, as well as to demonstrate this mechanism specifically in NPC. The use of integrated multi-omics analysis, alongside high-resolution structural evaluation, provides a comprehensive view of ANLN's oncogenic role. Moreover, the identification of ribosome biogenesis as an ANLN-dependent process offers a potential therapeutic vulnerability, particularly given the growing interest in therapeutically targeting nucleolar function in cancer.

Nonetheless, our study has limitations. The specific molecular mediators by which ANLN exerts its effects on nucleolar structure and function remain to be identified. The sample size of clinical specimens was relatively small, and prospective validation in larger, independent cohorts is warranted. Additionally, although we identified ribosome biogenesis as a downstream pathway, we did not investigate whether ANLN regulates transcriptional initiation of rDNA, post-transcriptional processing, or nucleolar assembly directly or indirectly.

Future research should focus on identifying ANLN-interacting partners in the nucleolus, mapping its genomic occupancy near ribosomal DNA loci, and determining whether its role is conserved across other tumor types. It will also be of interest to explore whether targeted inhibition of ANLN or its downstream effectors can suppress ribosome biogenesis and inhibit NPC progression in preclinical models.

In summary, this study demonstrates that ANLN is significantly overexpressed in nasopharyngeal carcinoma and correlates with poor clinical outcomes. Functional experiments reveal that ANLN promotes NPC cell proliferation and tumor growth, both *in vitro* and *in vivo*. ANLN knockdown was associated with reduced ribosome biogenesis and protein synthesis, indicating a potential regulatory role between ANLN and cellular biosynthetic capacity in NPC. These findings identify ANLN as a novel oncogenic driver in NPC and support the potential of targeting ANLN as a promising therapeutic strategy to inhibit tumor progression.

Acknowledgements: This study was supported by the National Natural Science Foundation of China (Grant No. 82360220), and the Natural Science Foundation of Jiangxi Province (Grant Nos. 20224BAB216050 and 20232BAB206078).

We thank all participating patients and research team members for their support.

Supplementary data are available in the online version of the paper.

References

[1] CHEN YP, CHAN ATC, LE QT, BLANCHARD P, SUN Y et al. Nasopharyngeal carcinoma. Lancet 2019; 394: 64-80. https://doi.org/10.1016/S0140-6736(19)30956-0

[2] LONG Z, WANG W, LIU W, WANG F, MENG S et al. Trend of nasopharyngeal carcinoma mortality and years of life lost in China and its provinces from 2005 to 2020. Int J Cancer 2022; 151: 684-691. https://doi.org/10.1002/ijc.33998

[3] WONG KCW, HUI EP, LO KW, LAM WKJ, JOHNSON D et al. Nasopharyngeal carcinoma: an evolving paradigm. Nat Rev Clin Oncol 2021; 18: 679-695. https://doi.org/10.1038/s41571-021-00524-x

[4] YANG Q, CAI Y, QIU S, ZHANG A. Integrated analysis of abnormal metabolic homeostasis for decoding tum or microenvironment. Front Mol Biosci 2024; 11. https://doi.org/10.3389/fmolb.2024.1443642

[5] YU J, PHAM TT, WANDREY N, DALY M, KARAM SD. Multimodality Management of EBV-Associated Nasopharyngeal Carcinoma. Cancers (Basel) 2021; 13: 6078. https://doi.org/10.3390/cancers13236078

[6] BUDNAR S, HUSAIN KB, GOMEZ GA, NAGHIBOSADAT M, VARMA A et al. Anillin Promotes Cell Contractility by Cyclic Resetting of RhoA Reside nce Kinetics. Dev Cell 2019; 49: 894-906.e12. https://doi.org/10.1016/j.devcel.2019.04.031

[7] CARIM SC, KECHAD A, HICKSON GRX. Animal Cell Cytokinesis: The Rho-Dependent Actomyosin-Anilloseptin Con tractile Ring as a Membrane Microdomain Gathering, Compressing, and So rting Machine. Front Cell Dev Biol 2020; 8: 575226. https://doi.org/10.3389/fcell.2020.575226

[8] GARNO C, IRONS ZH, GAMACHE CM, MCKIM Q, REYES G et al. Building the cytokinetic contractile ring in an early embryo: Initiati on as clusters of myosin II, anillin and septin, and visualization of a septin filament network. PLoS One 2021; 16: e0252845. https://doi.org/10.1371/journal.pone.0252845

[9] GUO E, MAO X, WANG X, GUO L, AN C et al. Alternatively spliced ANLN isoforms synergistically contribute to the progression of head and neck squamous cell carcinoma. Cell Death Dis 2021; 12: 764. https://doi.org/10.1038/s41419-021-04063-2

[10] WANG A, DAI H, GONG Y, ZHANG C, SHU J et al. ANLN-induced EZH2 upregulation promotes pancreatic cancer progression by mediating miR-218-5p/LASP1 signaling axis. J Exp Clin Cancer Res 2019; 38: 347. https://doi.org/10.1186/s13046-019-1340-7

[11] WANG D, NAYDENOV NG, DOZMOROV MG, KOBLINSKI JE, IVANOV AI. Anillin regulates breast cancer cell migration, growth, and metastasis by non-canonical mechanisms involving control of cell stemness and di fferentiation. Breast Cancer Res 2020; 22: 3. https://doi.org/10.1186/s13058-019-1241-x

[12] WU S, NITSCHKE K, HEINKELE J, WEIS CA, WORST TS et al. ANLN and TLE2 in Muscle Invasive Bladder Cancer: A Functional and Clinical Evaluation Based on In Silico and In Vitro Data. Cancers (Basel) 2019; 11: 1840. https://doi.org/10.3390/cancers11121840

[13] ZHU X, ZHANG Y, BIAN R, ZHU J, SHI W et al. ANLN Promotes the Proliferation and Migration of Gallbladder Cancer Cells via STRA6-Mediated Activation of PI3K/AKT Signaling. Cancers (Basel) 2024; 16: 752. https://doi.org/10.3390/cancers16040752

[14] Zheng H, Cheng ZJ, Liang B, Wang ZG, Tao YP et al. N^6-Methyladenosine Modification of ANLN Enhances Hepatocellular Carcinoma Bone Metastasis. Int J Biol Sci 2023; 19: 1009-1023. https://doi.org/10.7150/ijbs.73570

[15] SHORE D, ALBERT B. Ribosome biogenesis and the cellular energy economy. Curr Biol 2022; 32: R611-R617. https://doi.org/10.1016/j.cub.2022.04.083

[16] KANG J, BRAJANOVSKI N, CHAN K, XUAN J, PEARSON R et al. Ribosomal proteins and human diseases: molecular mechanisms and targeted therapy. Signal Transduct Target Ther 2021;6: 323. https://doi.org/10.1038/s41392-021-00728-8

[17] BURSAĆ S, PRODAN Y, PULLEN N, BARTEK J, VOLAREVIĆ S. Dysregulated Ribosome Biogenesis Reveals Therapeutic Liabilities in Cancer. Trends Cancer 2021; 7: 57-76. https://doi.org/10.1016/j.trecan.2020.08.003

[18] ZISI A, BARTEK J, LINDSTRÖM MS. Targeting Ribosome Biogenesis in Cancer: Lessons Learned and Way Forward. Cancers (Basel) 2022; 14: 2126. https://doi.org/10.3390/cancers14092126

[19] HWANG SP, DENICOURT C. The impact of ribosome biogenesis in cancer: from proliferation to metastasis. NAR Cancer 2024; 6: zcae017. https://doi.org/10.1093/narcan/zcae017
[20] CHANDRASHEKAR DS, BASHEL B, BALASUBRAMANYA SAH, CREIGHTON CJ, PONCE-RODRIGUEZ I et al. UALCAN: A Portal for Facilitating Tumor Subgroup Gene Expression and S urvival Analyses. Neoplasia 2017; 19: 649-658. https://doi.org/10.1016/j.neo.2017.05.002
[21] CHANDRASHEKAR DS, KARTHIKEYAN SK, KORLA PK, PATEL H, SHOVON AR et al. UALCAN: An update to the integrated cancer data analysis platform. Neoplasia 2022; 25: 18-27. https://doi.org/10.1016/j.neo.2022.01.001
[22] BARRETT T, WILHITE SE, LEDOUX P, EVANGELISTA C, KIM IF et al. NCBI GEO: archive for functional genomics data sets--update. Nucleic Acids Res 2013; 41: D991-995. https://doi.org/10.1093/nar/gks1193
[23] TUAN NM, LEE CH. Role of Anillin in Tumour: From a Prognostic Biomarker to a Novel Target. Cancers (Basel)2020; 12: 1600. https://doi.org/10.3390/cancers12061600
[24] TIAN D, DIAO M, JIANG Y, SUN L, ZHANG Y et al. Anillin Regulates Neuronal Migration and Neurite Growth by Linking Rho G to the Actin Cytoskeleton. Curr Biol2015; 25: 1135-1145. https://doi.org/10.1016/j.cub.2015.02.072
[25] WU S, NITSCHKE K, HEINKELE J, WEIS CA, WORST TS et al. ANLN and TLE2 in Muscle Invasive Bladder Cancer: A Functional and Clin ical Evaluation Based on In Silico and In Vitro Data. Cancers (Basel) 2019; 11: 1840. https://doi.org/10.3390/cancers11121840
[26] WANG A, DAI H, GONG Y, ZHANG C, SHU J et al. ANLN-induced EZH2 upregulation promotes pancreatic cancer progression by mediating miR-218-5p/LASP1 signaling axis. J Exp Clin Cancer Res 2019; 38: 347. https://doi.org/10.1186/s13046-019-1340-7
[27] WANG D, NAYDENOV NG, DOZMOROV MG, KOBLINSKI JE, IVANOV AI. Anillin regulates breast cancer cell migration, growth, and metastasis by non-canonical mechanisms involving control of cell stemness and differentiation. Breast Cancer Res 2020; 22: 3. https://doi.org/10.1186/s13058-019-1241-x
[28] ZHANG X, LI L, HUANG S, LIAO W, LI J et al. Comprehensive Analysis of ANLN in Human Tumors: A Prognostic Biomarker Associated with Cancer Immunity. Oxid Med Cell Longev 2022: 2022: 5322929. https://doi.org/10.1155/2022/5322929
[29] BUHAGIAR A, MCCOOL M, BRYANT C, ABRIOLA L, SUROVTSEVA Y et al. Human pre-60S assembly factors link rRNA transcription to pre-rRNA processing. RNA 2022; 29: 82-96. https://doi.org/10.1101/2022.03.01.482553
[30] RIBACK J, EEFTENS J, LEE D, QUINODOZ S, DONLIC A et al. Viscoelasticity and advective flow of RNA underlies nucleolar form and function. Mol Cell 2023; 83: 3095-3107. https://doi.org/10.1016/j.molcel.2023.08.006
[31] BROWN I, NAVARRO ML, HAO YH, CONACCI-SORRELL M. ZNF692, a novel nucleolar regulator in cancer. The FASEB Journal 2022; 36. https://doi.org/10.1096/fasebj.2022.36.s1.l7982
[32] FERREIRA R, HANNAN KM, PANOV K, UDUMANNE T, GEORGE AJ et al. Second generation RNA Polymerase I inhibitor PMR-116 targets ribsomal RNA synthesis to potently treat a broad spectrum of malignancies. Mol Cancer Ther 2024; 23: PR004. https://doi.org/10.1158/1538-8514.rnadrivers24-pr004

Figure Legends

Figure 1. ANLN is overexpressed in multiple cancers and is associated with poor prognosis in NPC. A) mRNA expression levels of ANLN in 24 cancer types and corresponding normal tissues based on TCGA data. B) Protein expression levels of ANLN in 10 cancer types and corresponding normal tissues from CPTAC data. C) ANLN expression in NPC and normal tissues from the GSE12452 dataset. D) ANLN expression in NPC and normal tissues from the GSE61218 dataset. E) Distribution of clinical stages between high and low ANLN expression groups in the GSE102349 dataset. F) Kaplan-Meier overall survival analysis of patients with high and low ANLN expression in the GSE102349 dataset.

Figure 2. ANLN is highly expressed in NPC cell lines and clinical specimens. A) mRNA expression levels of ANLN in the normal nasopharyngeal epithelial cell line (NP69) and various NPC cell lines. B, C) Protein expression levels of ANLN in NP69 and NPC cell lines as determined by Western blot analysis. D) Immunohistochemical staining of ANLN in NPC tissues and adjacent normal tissues; black scale bar=100 μm. E) Quantitative IHC scores comparing ANLN expression in NPC tissues and adjacent normal tissues. Each grey line connects values from the same patient (n=6 pairs).

Figure 3. Knockdown of ANLN inhibits NPC cell proliferation *in vitro*. A, B) Western blot analysis confirming the knockdown efficiency of ANLN protein expression in NPC cells. C) CCK-8 assay showing cell proliferation at different time points after ANLN knockdown. D, E) Colony formation assay evaluating the clonogenic ability of NPC cells following ANLN knockdown.

Figure 4. Knockdown of ANLN inhibits tumor growth *in vivo*. A) Representative images of xenograft tumors from each group. B) Statistical analysis of tumor weights at the end of the experiment. C) Body weight curves of nude mice during the observation period. D) Tumor growth curves showing tumor volume over time. E) Immunohistochemical staining of ANLN and Ki-67 in tumor tissues; black scale bar=100 μm.

Figure 5. Knockdown of ANLN impairs ribosome biogenesis and protein synthesis. A) Gene Set

Enrichment Analysis (GSEA) showing that ANLN knockdown significantly suppresses ribosome biogenesis pathways. B) Reduced protein synthesis efficiency after ANLN knockdown, as assessed by puromycin incorporation assay. C) Altered nucleolar morphology in ANLN-depleted cells observed by TEM. D) Decreased number of ribosomal granules following ANLN knockdown. Black scale bar in (C) and (D)=500 nm.

Fig. 1 [Download full resolution image]

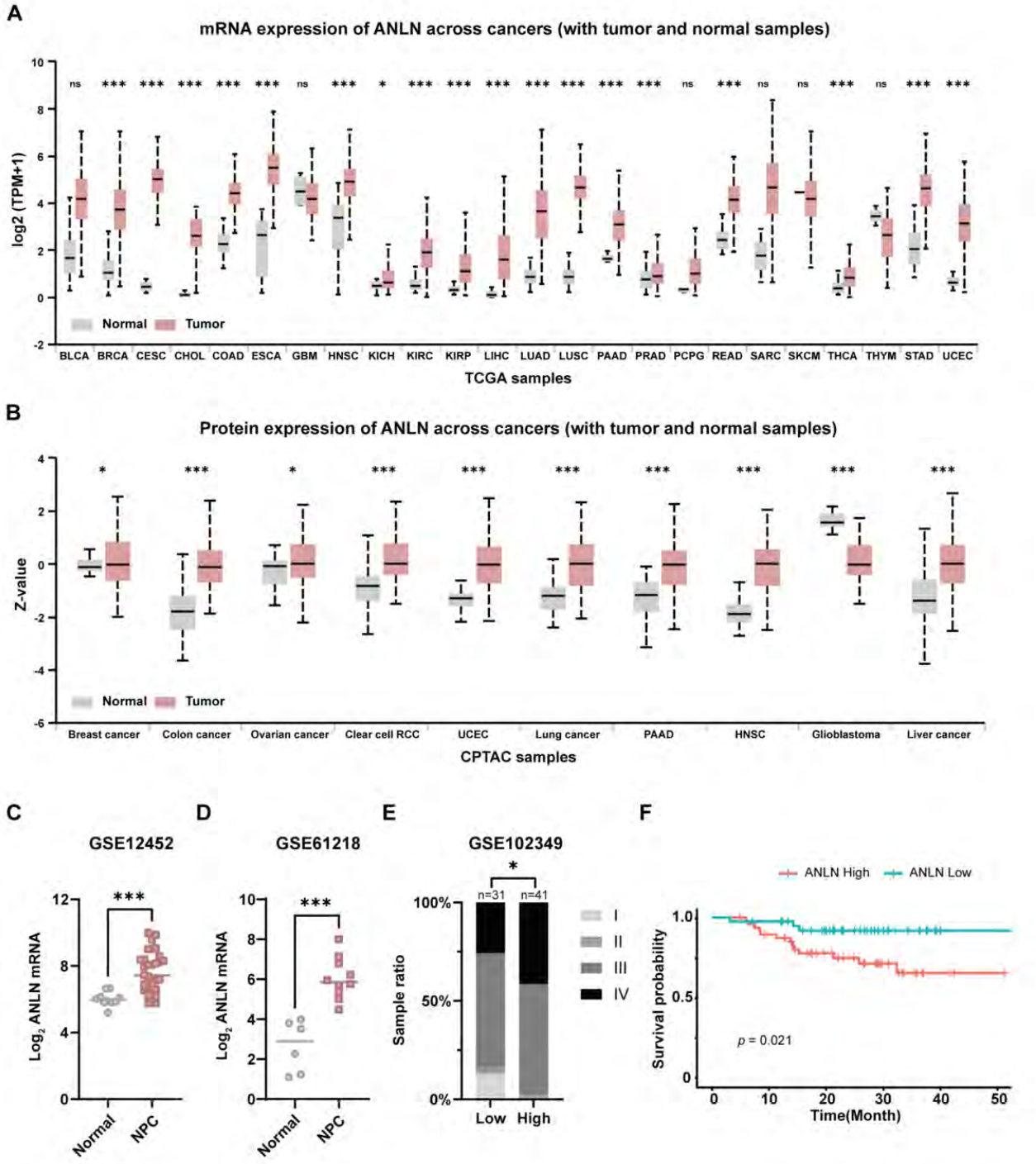

Fig. 2 [Download full resolution image]

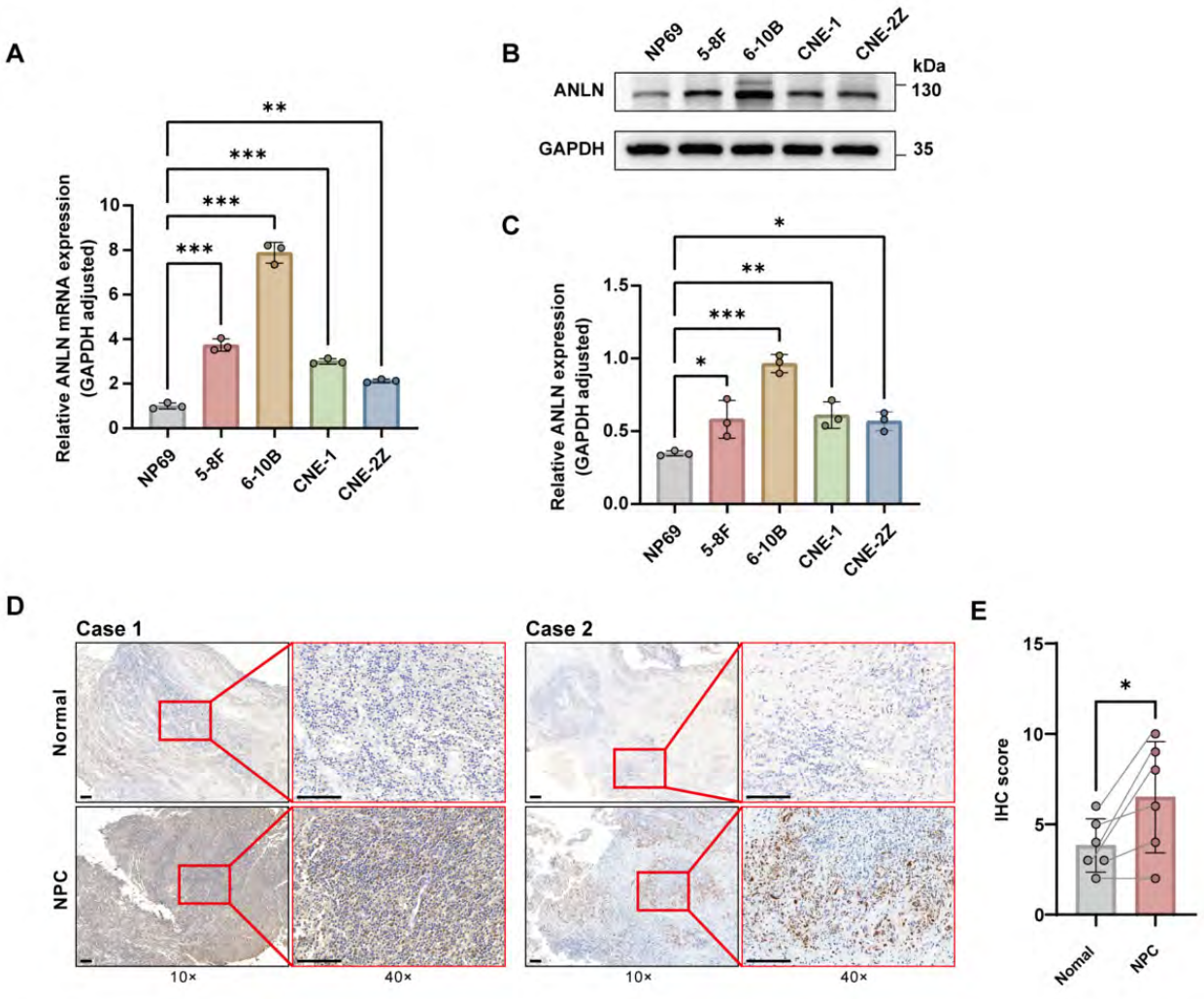

Fig. 3 [Download full resolution image]

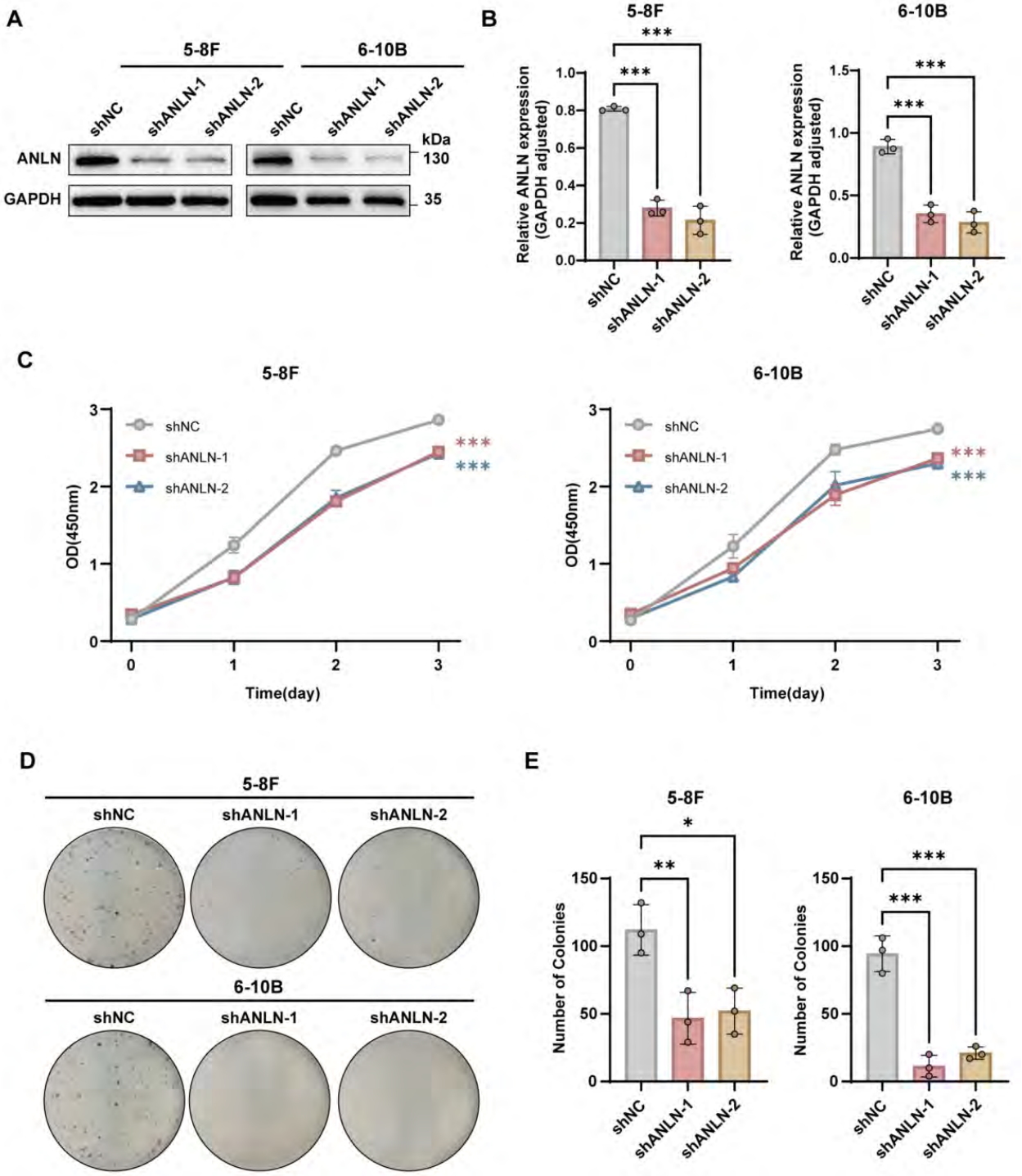

Fig. 4 [Download full resolution image]

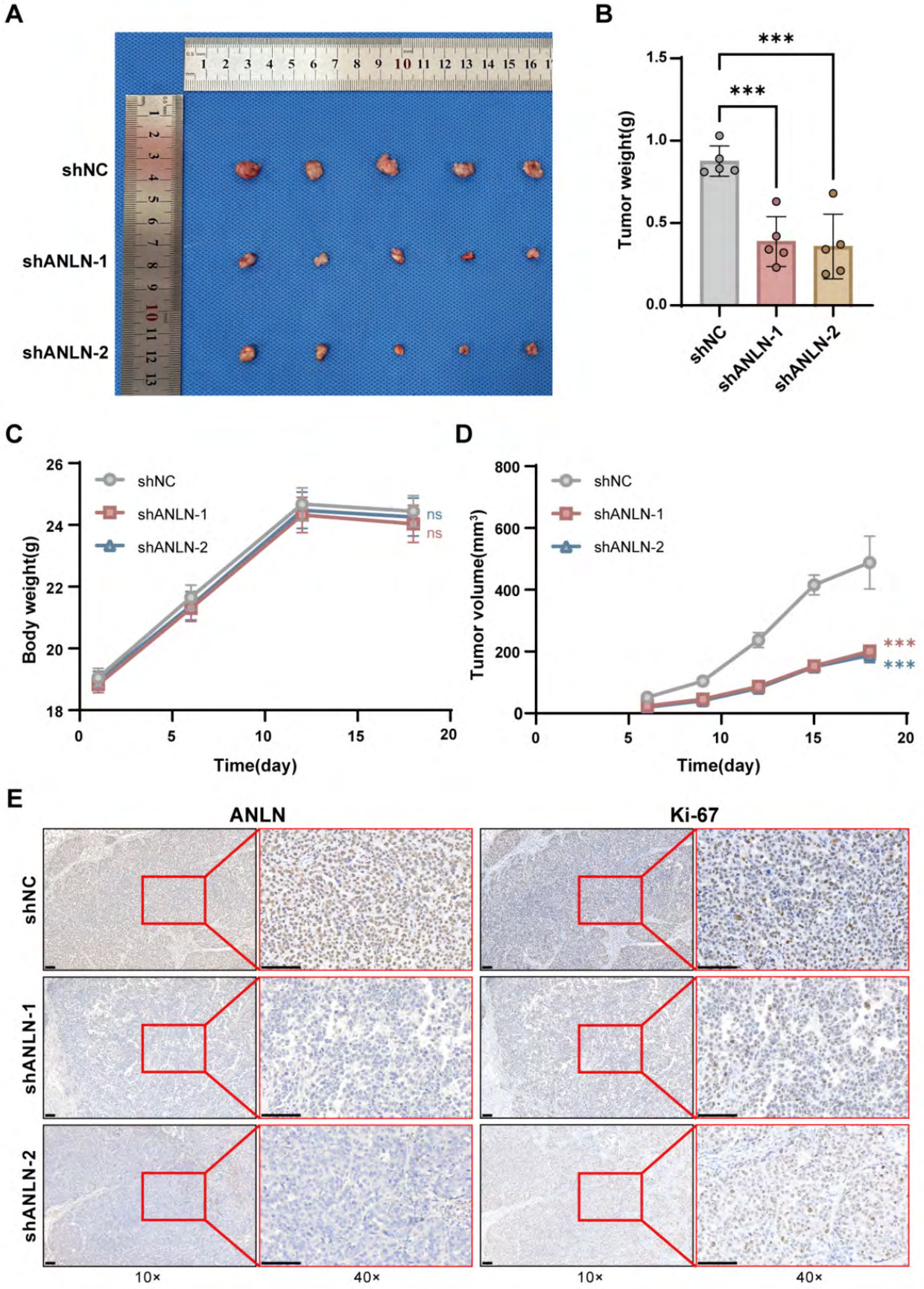

Fig. 5 [Download full resolution image]